MATERIALS SCIENCE

# Significant and stable drag reduction with air rings confined by alternated superhydrophobic and hydrophilic strips

Haibao Hu,[1]* Jun Wen,[1] Luyao Bao,[1] Laibing Jia,[1] Dong Song,[1] Baowei Song,[1] Guang Pan,[1] Michele Scaraggi,[2,3] Daniele Dini,[3]* Qunji Xue,[4] Feng Zhou[4]*



**Superhydrophobic surfaces have the potential to reduce the viscous drag of liquids by significantly decreasing friction at a solid-liquid interface due to the formation of air layers between solid walls and interacting liquids. However, the trapped air usually becomes unstable due to the finite nature of the domain over which it forms. We demonstrate for the first time that a large surface energy barrier can be formed to strongly pin the three-phase contact line of air/water/solid by covering the inner rotor of a Taylor-Couette flow apparatus with alternating superhydrophobic and hydrophilic circumferential strips. This prevents the disruption of the air layer, which forms stable and continuous air rings. The drag reduction measured at the inner rotor could be as much as 77.2%. Moreover, the air layers not only significantly reduce the strength of Taylor vortexes but also influence the number and position of the Taylor vortex pairs. This has strong implications in terms of energy efficiency maximization for marine applications and reduction of drag losses in, for example, fluid transport in pipelines and carriers.**

## INTRODUCTION

In the past decades, to maximize the energy efficiency and enhance the traveling speed and distance of underwater and naval vehicles, as well as to minimize the drag losses in fluid transport in pipelines, researchers have made tremendous efforts to develop methods (*1*–*3*) to reduce wall frictional drag, which accounts for a large proportion of the total dissipation of well-designed underwater vehicles. Inspired by the fact that an object moving in air experiences much smaller drag force than in water, due to the large dynamic viscosity contrast between water and air, scientists and engineers have invented different ways to create an air layer covering the vehicles moving in water, thus reducing frictional drag (*1*, *2*). Through the application of air cushioning, the solid-liquid interface is replaced by a solid-gas interface, which reduces the wall frictional drag significantly.

One of those attempted methods involves injecting air in the boundary layer, leading to drag reduction (DR) between 25 and 80% of the nominal drag (*4*–*8*). In the presence of limited air flux, air bubbles decrease the average density and viscosity of the fluid in the boundary layer, thereby modifying the transport of momentum and reducing drag. When the air flux is sufficiently high, the air bubbles coalesce into a continuous air layer (air cushioning), which fully separates the water flow and the solid surface, resulting in much larger DR. The utilization of superhydrophobic surfaces to force the injected air to remain attached to the wall has also been investigated (*9*). Another way to form thick air layers in the proximity of the wall is through the generation of cavities (*1*, *10*, *11*), which result from the vaporization of the surrounding water (called vaporous cavities) (*12*) and normally require a large free-stream speed. By continuously injecting air, the required free-stream speed to sustain the cavity (called a ventilated cavity in this case) (*11*, *13*) decreases moderately. The use of superhydrophobic surfaces to form a microscopic air layer that prevents direct fluid/solid contact has also been extensively studied (*2*, *14*–*20*). It is widely accepted that the geometry and surface energy distribution of the micro- and nanoscale structures, characterizing a generic superhydrophobic surface, may prevent water from penetrating into the space between them (leading to a Cassie-Baxter wetting regime). Therefore, numerous air/water menisci form between the surface roughness and lead to DR. However, it has been shown that, under certain conditions, this can also lead to drag increase (DI) (*21*–*25*), for example, when superhydrophobic surfaces are combined with microridges aligned normal to the flow direction; this corresponds to the air-water interface penetrating and potentially disrupting the flow or to the reduction of the air layer. The magnitude of DR or DI is dictated not only by the slip length [which is governed by the wetting state of the surface, the continuity and shape of the air-water interface, and the wetted solid fraction (*14*, *26*–*29*)] but also by the local fluid dynamics occurring near the macroscopically nonwetting interface. Very similar effects have been found in terms of friction reduction and hydrodynamic load support in textured bearings (*30*–*33*).

DI may be induced by a transition from Cassie-Baxter wetting regime to Wenzel regime that significantly increases the contact area. This is also the reason why the maximum DR is obtained by air injection systems. Therefore, the reliability of DR obtained using superhydrophobic surfaces needs to be improved. To this end, the ideal design is one that produces stable and continuous air cushioning layers and exploits the nonwetting properties of superhydrophobic coatings. A recent contribution has shown how the "Leidenfrost" effect, achieved by active heating, can be used to sustain a stable air layer on the superhydrophobic surface, and a 90% DR was achieved (*34*). Here, we propose a new methodology of using alternating superhydrophobic/hydrophilic strips to passively create and maintain a stable air layer with a thickness of hundreds of micrometers in Taylor-Couette (TC) water flow. The air layer has no pinning structures along the flow direction but is strongly pinned normal to the flow direction, and an unprecedented DR is achieved without any air supply during flow. The DR is very similar to the best result that can be achieved by air feeding systems (~80%). In comparison, the unpatterned superhydrophobic surface only shows a much smaller DR (less than 15%) under the same flow conditions.

[1]School of Marine Science and Technology, Northwestern Polytechnical University, Xi'an 710072, China. [2]Department of Engineering for Innovation, Universitá del Salento, 73100 Monteroni-Lecce, Italy. [3]Department of Mechanical Engineering, Imperial College London, South Kensington Campus, Exhibition Road, London SW7 2AZ, UK. [4]State Key Laboratory of Solid Lubrication, Lanzhou Institute of Chemical Physics, Chinese Academy of Sciences, Lanzhou 730000, China.
*Corresponding author. Email: huhaibao@nwpu.edu.cn (H.H.); d.dini@imperial.ac.uk (D.D.); zhouf@licp.cas.cn (F.Z.)

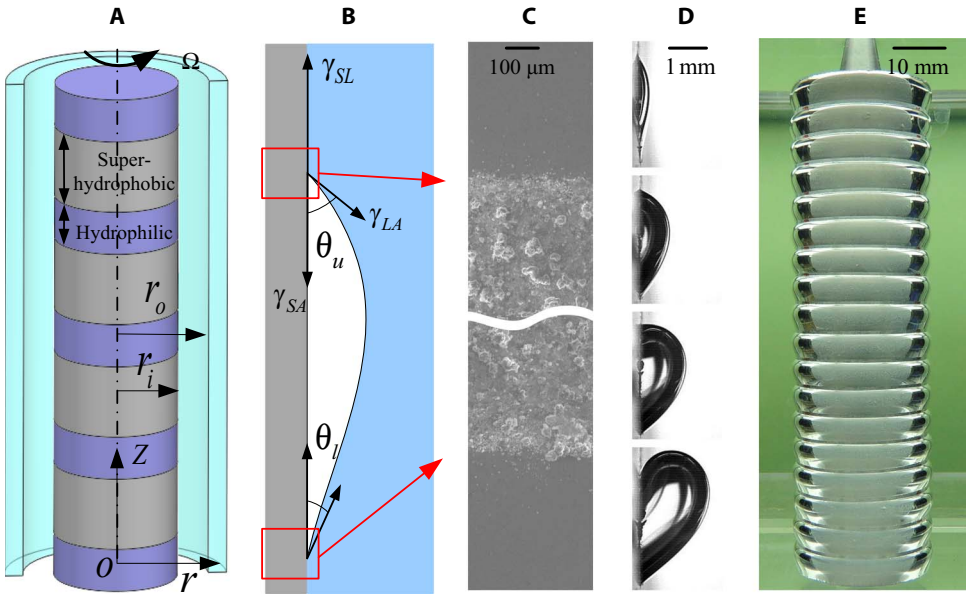


**Fig. 1. Schematics and pictures describing the physical principles governing the interactions between air bubbles and textured surfaces in the Taylor-Couette apparatus.** (**A**) Schematic of the test apparatus. (**B**) Schematic cross-sectional profile of an air bubble on a vertical plate. (**C**) SEM of the jointed superhydrophobic (pho) and hydrophilic (phi) surfaces. (**D**) Cross-sectional view of air bubbles sticking on superhydrophobic circular spots at the center of the hydrophilic plate—shown as a reference to introduce the concept of air bubble pinning (note that this is not the test configuration discussed in this investigation). The upper air contact angle (defined as the angle measured through the air, where an air-water interface meets a solid surface), $\theta_u$, of the air bubble ranges from ~27° to ~140° (from top to bottom) because of the surface energy barrier needed for the bubble to unpin from the substrate and due to the discontinuity in the surface energy. (**E**) Inner rotor of the TC cell showing the actual air rings generated in our experimental apparatus.

The experimental setup (see Methods) used to prove the effect of the trapped air layers on DR, determined by the alternation of superhydrophobic and hydrophilic surface strips, is depicted schematically in Fig. 1A. Similar methods based on the use of a TC apparatus for DR investigations have been reported in the recent literature (*20*, *34*, *35*). Here, an inner cylinder (radius $r_i$) is subjected to a steady rotation (with angular speed Ω) with respect to an outer cylinder (radius $r_o$). The gap between the cylinders is filled with water, and the inner cylinder is textured with alternating superhydrophobic and hydrophilic strips, which continuously cover the rotor in the circumferential direction. We note first that topographical (but also chemical) heterogeneities uniformly distributed over a solid surface form a locus of pinning sites (local discontinuities) for a bubble; thus, whenever air is entrapped and a three-phase contact line is produced on such discontinuities, the air contact angle hysteresis (*36*, *37*) will characterize the contact line movements. The air contact angle hysteresis is generally defined as $\Delta\theta = \theta_A - \theta_R$, where $\theta_A$ and $\theta_R$ are the advancing and receding air contact angles, respectively; however, here, these two angles are identified using the notation $\theta_u$ and $\theta_l$, respectively, to identify the upper and lower air contact angle considering buoyancy-induced deviations (see Fig. 1B). It should be noted that the contact angle of the air bubble is used, which provides a better characterization of the geometry of the air bubble at the three-phase contact line than the water contact angle; also, in accordance to other contributions in this research field, we still use the nomenclature "hydrophilic" and "superhydrophobic" to indicate the behavior of the alternated wetting strips, although for a rigorous definition one should describe them as aerophobic and aerophilic, respectively. In order for the bubble to move from the pinned state on a planar surface, the contact line has to overcome an energy barrier, whose strength can be expressed by the threshold capillary force $F_{max} = \gamma_{LA} l(\cos\theta_R - \cos\theta_A)_{max}$ for the two-dimensional contact case (*38*), where $\gamma_{LA}$ is the air/water surface tension and $l$ is the length of the contact line (*39*, *40*). However, the threshold capillary force of a nominally spherical air bubble, formed on the superhydrophobic surface, is typically extremely low (corresponding to a representative air contact angle hysteresis in the plane of symmetry below 5° to 10°) (*41*, *42*); this can be expected for different reasons, including the fact that the spherical bubble pinning front is curvilinear, and its pinning action is not entirely aligned with the sliding direction. Therefore, the attainable capillary force is small, and any air bubble (deposited onto the substrate) can easily flow away due to, for example, its buoyancy or the shear force exerted by the water flow (*9*).

A large energy barrier to stop the movement of the bubble is formed here by interposing hydrophilic (phi) surfaces (that is, aerophobic) between superhydrophobic (pho) (that is, aerophilic) surfaces. It is shown in Fig. 1D, which is simply used for illustrative purposes, that the air contact angle hysteresis at the boundary between superhydrophobic and hydrophilic surfaces is very large only in the plane of symmetry of the bubble (>110°) and that the corresponding three-phase contact line is stably formed in a macroscopic configuration. Using this principle, a number of alternately arranged superhydrophobic/hydrophilic strips are prepared (see Methods) on the surface of the rotor to create a two-dimensional bubble line contact, which extends to the entire circumference of the rotor and is always orthogonal to its axis. By slowly injecting air onto the superhydrophobic strips using a microsyringe, annular air bubbles (called air rings) are formed and suspended along the surface of the rotor. A full view of the inner rotor of the experimental apparatus showing fully developed air rings is displayed in Fig. 1E. In contrast with the ordinary thin air layer that forms on superhydrophobic surfaces and is sustained by the microstructural features of the surface roughness (*43*–*45*), the air rings are

sustained by the stability of the three-phase contact line and the air/water surface tension. The annular air rings present a continuous circumferential bubble pinning boundary along the flow direction when the rotor spins.

## RESULTS

### Air rings shape

The air rings deform and change shapes depending on the surface design and running conditions; therefore, the rotation rates are systematically varied to measure the torque contribution of the TC flow, $T$, on the inner rotor, with annular air rings having different widths and thicknesses. The width of the hydrophilic strip $w_{phi} = 1 \pm 0.05$ mm is constant, whereas the width of the superhydrophobic surface $w$ ranges from 2 to 6 mm. The average radial thickness of the air ring is defined as $TH = \sqrt{(V + \pi w_{pho} r_i^2)/\pi w_{pho}} - r_i$, where $V$ is the air injected volume (see the inset at the bottom right of Fig. 2).

Figure 2A provides a comparison between the predicted bubble shape in the meridian plane (red curves, see section S1) and the optical acquisition (dark region, see Methods) of the air rings for a superhydrophobic strip of 4 mm and for $r_i = 12.5$ mm. The agreement is well within the experimental accuracy in determining the injected air volume. It should be observed that for the lower volume (0.05 ml), the predicted bubble axial thickness is $w_b = 0.35$ mm, less than the size of the superhydrophobic strip. During the air injection process, the air bubble first nucleates and pins on the upper border of the strip (I). Upon further air injection, the bubble grows toward the lower end of the strip to finally pin at the lower hydrophobic strip border (II). Consequently, by further air injection, the bubble grows along the radial direction (III and IV) until the unstable equilibrium configuration is reached. Because of the buoyancy, the cross section of the air ring is generically curvilinear, as shown in Fig. 2A, and its exact shape depends on different parameters, as discussed in section S1. Each air ring has different upper, $\theta_u$, and lower, $\theta_l$, air contact angles, thus forming a capillary force $F$, which equilibrates the buoyancy $F_B$, with $F_B = F = \gamma_{LA} l(\cos\theta_l - \cos\theta_u)$, where the length of the contact line is $l = 2\pi r_i$. When $\theta_u$ reaches its critical value, $\theta_{Cr}$, the air ring reaches its maximum volume, leading to $V_{max} = \gamma_{LA} l(\cos\theta_l - \cos\theta_{Cr})/\rho g$. The maximum volume of air in an air ring formed on a 4-mm-width superhydrophobic strip under static water measured in this study is 0.36 ml.

Figure 2B shows the simulated bubble shape and its evolution in terms of slip states as a function of the hydrophobic strip size (points A to E), $w_{pho}$, for constant bubble thickness, TH. At constant air ring thickness, the increase of the bubble axial size $w_b$ is not linearly proportional to the superhydrophobic strip size $w_{pho}$. Therefore, in correspondence to the largest values of $w_{pho}$, the bubble only partially extends over the hydrophobic domain (Fig. 2B: C to E), which is thus wet in a generic Cassie-Baxter regime. As we will see in the following, the existence of this partial wetting regime will strongly affect the drag and, therefore, the measured torque. The bottom of Fig. 2B shows the theoretical prediction of the bubble axial length $w_b$ as a function of the hydrophobic strip size, $w_{pho}$, for different air ring thicknesses, namely, TH = 0.16, 0.31, 0.47, and 0.62 mm, and for $r_i = 12.5$ mm. This has been obtained using the analytical model described in section S1.

The role of the Bond number $B_o = (w_b/l_c)^2$, where $l_c = \sqrt{\gamma_{LA}/(\rho g)}$, in the bubble formation and shape evolution predicted by simulations

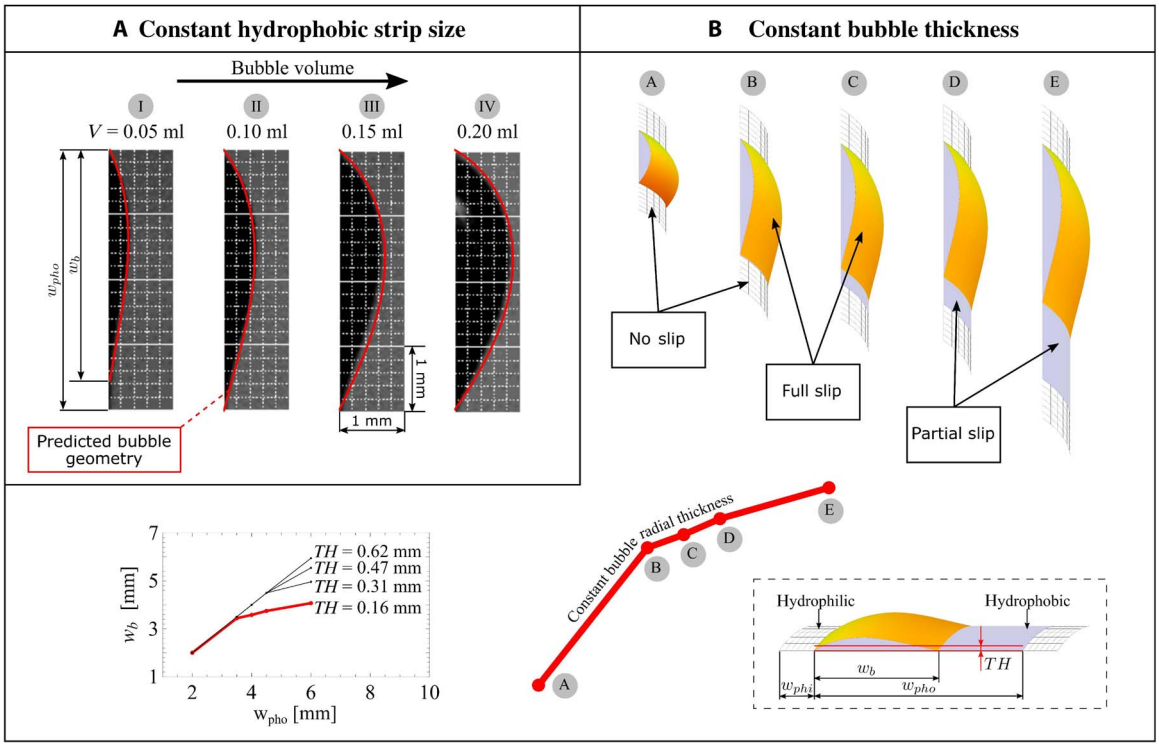


**Fig. 2. Experimental visualization and comparison with theoretical predictions of the air ring shape in static configurations.** (**A**) Bubble geometry in the meridian plane as predicted by simulations (red curves, see section S1) and measured through optical acquisitions (dark region, see Methods) for a superhydrophobic strip of 4 mm and for the internal cylinder radius $r_i = 12.5$ mm. (**B**) Simulated bubble shape as a function of the hydrophobic strip size, $w_{pho}$, for constant bubble thickness, TH; the graph inset (right) shows the outcomes of the simulations in terms of predicted bubble axial length, $w_b$, and configuration as a function of the hydrophobic strip size, $w_{pho}$, for different values of the bubble thickness, TH.

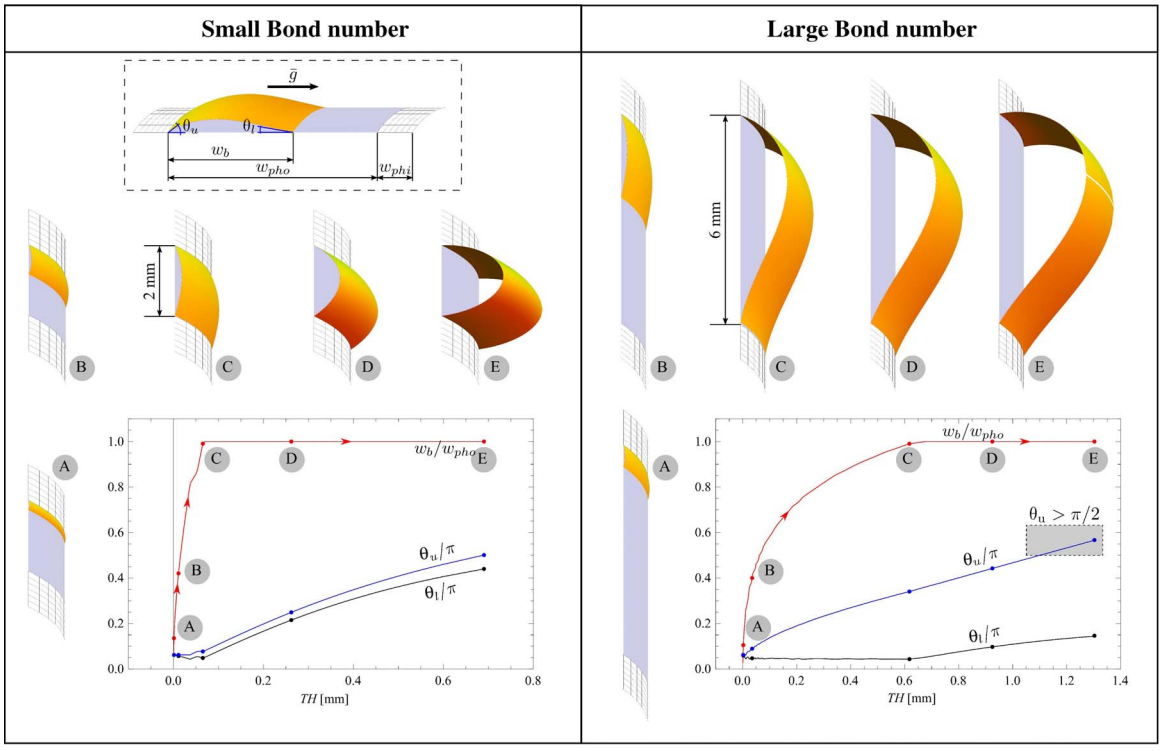


**Fig. 3. Theoretical investigation of the effect of Bond number $(w_b/l_c)^2$, where $l_c = \sqrt{\gamma_{LA}/(\rho g)}$, on the bubble formation and shape evolution obtained numerically (see section S1).** (**Left**) Small Bond numbers, with $w_{pho}$ = 2 mm. (**Right**) Large Bond numbers, with $w_{pho}$ = 6 mm. The curves in the graphs show, for a fixed $w_{pho}$, the normalized bubble growth along the axial direction, $w_b/w_{pho}$ (red curve), and the air contact angles ($\theta_u$ and $\theta_l$) as a function of the air injected volume; the latter is expressed in terms of the bubble equivalent thickness TH. The larger the Bond number, the larger the air contact angle hysteresis of the air ring, which corresponds to a decreasing value of receding air contact angle; thus, for large Bond numbers, a larger pinning strength can be provided because of the increasing value of $\cos\theta_l - \cos\theta_u$.

is shown in Fig. 3. Here, note that the case of large Bond number is characterized by a large discrepancy between the top and bottom bubble pinning angles, resulting in a larger asymmetry of the bubble profile with respect to the small Bond number circular shape. We will show in the section discussing measured torque and DR that the occurrence of this air ring asymmetry does not quantitatively affect the drag torque, thus making the friction process insensitive to the Bond number. Furthermore, in section S1, we show that the superposition of a centripetal acceleration, consequent to the application of a rotational speed to the textured cylinder, does not alter the bubble shape to any measurable extent. Thus, our air ring's design is demonstrated to be insensitive to the parametric variation of the interface physical properties, thus stably providing the cushioning effect as a tool to achieve significant DR.

Considering that the thickness of the air ring is critical to its DR ability (*43*), we assessed the effect of the compressibility and water solubility (in-water diffusion) of air on the time evolution of the air ring thickness (see section S6). For the air-saturated water used in this investigation, it was observed that the volume of the air ring changes by less than 2% in 4 hours when the inner rotor rotates at 20.9 rad/s. This indicates that the air rings are very stable.

## Measured torque and DR

The measured torque $T_m$ is the sum of two contributions, $T + T_b$. $T$ is the contribution coming from the flow in the proximity of the cylindrical surfaces, whereas $T_b$ is the torque given by both the top and bottom cylinder flat surfaces. Here, we measured $T_b$ using the same linearization method as that used by Greidanus *et al.* (*46*). This is done by measuring the torque of the inner rotor with different lengths submerged in water. In this process, $T_b$ (more precisely, half $T_b$) keeps constant, whereas the contribution of the side wall increases linearly with its submerged length. The results show that the measured ratio $T_b/T_m$ ranges from 0.12 to 0.13 for different rotating speeds.

Thus, we determined the contribution of the cylindrical surfaces, $T$, by subtracting the measured $T_b$ from the measured $T_m$. For each point, the torque $T_m$ is measured for a period of 30 s. Four tests are performed for each of the states, and the torque is averaged across all runs. The DR is defined as DR = $(T_s - T)/T_s \times 100\%$, where $T_s$ and $T$ are the cylinder torque contributions of the TC flow for smooth uncoated inner rotor and the results obtained in the presence of air rings, respectively.

As shown in Fig. 4, considerable DR is observed experimentally for all the inner rotors with air rings on them. The dimensionless torque $T'$ of the inner rotor increases with Reynolds number $Re_C$ following the power law of $T' \sim Re_C^n$, whereas the scaling exponent $n$ decreases from 1.44 ± 0.01 for smooth inner rotor to 1.32 ± 0.01 for inner rotor in the presence of fully formed air rings (Fig. 4, left). Here, $T' = T/(\rho\upsilon^2 L)$, $Re_C = r_i(r_o - r_i)\Omega/\upsilon$, where $\rho$ and $\upsilon$ are the density and kinematic viscosity of water, respectively. For all the inner rotors with air rings on them, up to 77.2% of DR is observed, and the DR varies within 2% in the range of Reynolds numbers tested (inset to Fig. 4, left). Furthermore, in Fig. 4 (right), the experiments conducted at constant Reynolds number show that the DR increases with the TH of the air ring. Instead, a maximum DR exists as a function of the hydrophobic strip axial length, $w_{pho}$, at constant TH of the air ring and at constant $w_{phi}$. Such a maximum can be justified as follows. For small $w_{pho}$, increasing $w_{pho}$ determines a proportional increase of the axial width of the air ring $w_b$, leading to a larger fraction of the inner rotor surface being covered by the slippery air

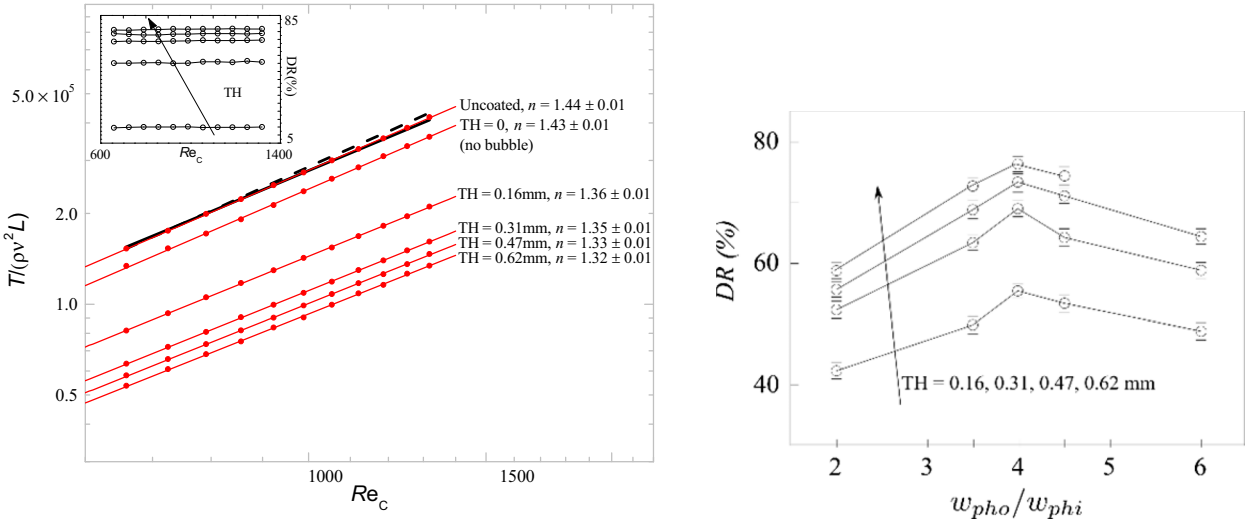


**Fig. 4. Experimental investigation of the effect of the Couette Reynolds number $Re_C$, air ring radial (TH), and axial ($w_{pho}/w_{phi}$) width on measured torque and DR obtained experimentally.** (**Left**) Variation of the dimensionless torque $T' = T/(\rho\upsilon^2 L)$ against $Re_C$ (red dots) for the uncoated inner rotor and for different bubble radial thickness (including the case of no air injection). The solid red lines represent the fit to the scaling $T' \sim Re_C^n$, and $n$ is the scaling exponent. The solid and dashed black lines represent the empirical power law describing the dimensionless torque for the transition and low-turbulent regime, respectively (the calculation methods are presented in section S3). Inset: Variation of the DR against $Re_C$. Results are measured for a constant value of $w_{pho}$ = 4 mm. (**Right**) DR as a function of the hydrophobic strip size for different equivalent radial widths (TH) of the air ring but at constant $Re_C$ = 1320.

bubble. Consequently, this leads to an improved DR and to a reduction of the effective azimuthal wall velocity $\bar{v}_0$ with respect to the externally applied cylinder azimuthal velocity $v_0$. Note that the effective azimuthal wall velocity $\bar{v}_0$ can be considered as the equivalent azimuthal velocity of the untextured cylinder ($\bar{v}_0 < v_0$ takes into account the air bubble slippage in the equivalent untextured TC flow) (see section S4). By further decreasing the effective azimuthal wall velocity $\bar{v}_0$ (thus increasing $w_{pho}$) a shift in the dynamics of the flow toward the laminar regime is observed, given that the effective Reynolds number ($\sim\bar{v}_0$) of the TC flow decreases. Because the generic TC flow regime is characterized by a torque scaling prefactor [the so-called modified torque coefficients in the study of Bilgen and Boulos (*47*)], which strongly increases toward the laminar regime, the further increase of $w_{pho}$ results in a reduced DR. This, in addition to the formation of partial bubble contact occurring at increasing $w_{pho}$ and leading to a reduced air ring coverage over the superhydrophobic strip, definitely provides a decrease of the DR, as observed experimentally in Fig. 4 (right). Therefore, influenced by these two factors, the DR curves show the existence of a maximum in correspondence of hydrophobic strip size of about 4 mm for our system.

## DISCUSSION

The results in terms of DR are analyzed with flow field simulations of the TC geometry at varying texture parameters, as presented in Fig. 5 (the calculation methods are presented in section S4). In particular, in Fig. 5, we show, on the top, the effect of bubble skewness (asymmetry due to large Bond numbers), bubble thickness (TH), bubble axial length ($w_b$), and hydrophobic textured area density ($\alpha$) on the predicted dimensionless torque ($\bar{C}$, defined in eq. S4.4; note that $\bar{C} = 1$ for the untextured case). Here, all the simulations are done assuming a full bubble contact over the hydrophobic strip ($w_{pho} = w_b$).

We note first that, for all the investigated cases, the smaller the effective azimuthal wall velocity $\bar{v}_0$, the smaller the dimensionless drag torque (in section S4, we show that both dimensionless torque and mean azimuthal flow velocity curves are qualitatively similar). Furthermore, we note that the bubble skewness has a negligible influence on the drag torque; the azimuthal velocity field is skewed too, but the smallest bubble-wall speeds are similar in the two cases. Moreover, we note that the strongest effects on the torque reduction are given by the increase of the patterned area density. However, when introducing the effect of the (more realistic) bubble partial contact (bottom panel), the incomplete contact introduces a geometric effect on the DR, which leads to the maximum in the curves shown in Fig. 4 (right).

Let us now focus on another aspect of the mechanisms responsible for the DR. First, it can be shown (see section S2) that, even for the thinnest air ring, the contribution to losses due to air-solid friction can be neglected, and therefore, solid-liquid friction accounts for most of the drag measured on the inner rotor. Because the air rings cover 80% of the vertical surface of the inner rotor, the DR based on $T$ would be expected to range from 74 to 78% for air rings with different TH. However, the measured DR only ranges from 56.6 to 77.2%. To shed light on the reasons for this discrepancy, the velocity distribution along the radial direction and radial-axial vorticity fields of the gap flow are measured.

Because the air-solid friction in the air ring is very small, the water between the air rings and the outer cylinder gets little azimuthal momentum from the air-water interface. Thus, there exists an azimuthal velocity gradient in the axial direction between the fluid flowing near the hydrophilic strips and the fluid in the proximity of the air rings. However, the intense viscous shear stress and Taylor vortexes developing in the flow lead to strong azimuthal momentum transport.

Because the azimuthal momentum generated in correspondence to the hydrophilic strips is transported to the fluid flowing near the air rings, the azimuthal velocity above the hydrophilic strips at the same radial position of the air-water interface is much lower than that generated for the equivalent case but with a smooth inner rotor (see the experimental results reported in Fig. 6A); this means that there is a larger velocity gradient ($\frac{du_\theta}{dr}$) at the inner rotor wall. Therefore, the shear stress

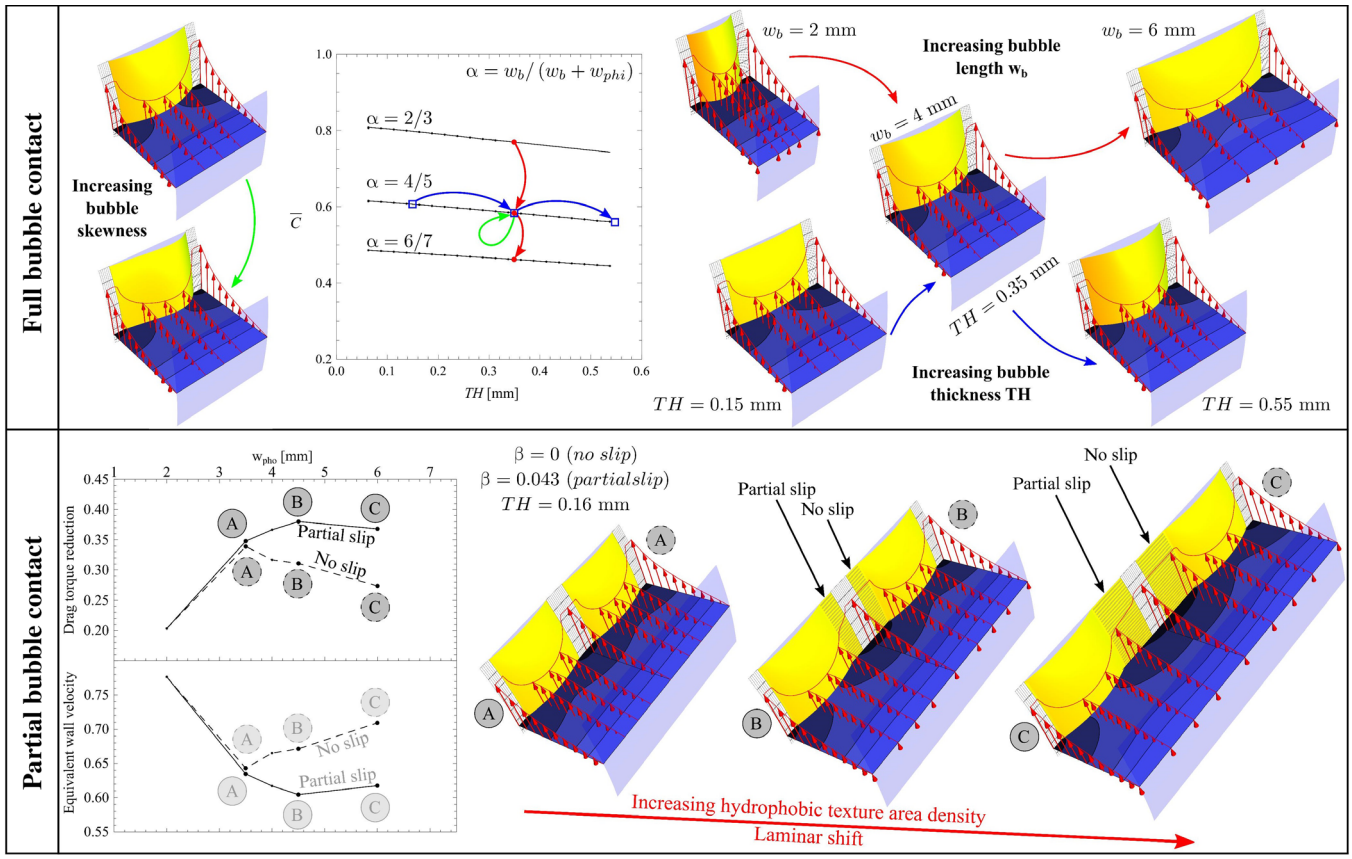


**Fig. 5. Theoretical investigation of the effect of flow strips, air ring behavior, and geometrical configuration on torque obtained numerically.** (**Top**) Dimensionless torque $\overline{C}$ (see section S4) as a function of the bubble thickness TH for different texture area density $\alpha$ and Bond numbers. In the calculations, we have considered the case $w_{pho} = w_b$ (bubble covering the whole hydrophobic strip), whereas the superhydrophobic/hydrophilic reference texture is characterized by TH = 0.35 mm and $w_b$ = 4 mm. Increasing the Bond number (green path) has no effect on the drag torque. Instead, increasing the texture area density $\alpha$ (red path) determines a net reduction of the water velocity on the bubble surface, resulting in a stronger reduction in the generated drag torque. The bubble thickness TH (blue path) has an influence similar to $\alpha$ but weaker in terms of reduction of the water speed on the bubble wall. (**Bottom**) Dimensionless drag torque reduction (and effective azimuthal wall velocity $\bar{v}_0$) as a function of the hydrophobic axial size $w_{pho}$ (here, $w_{pho} \geq w_b$) for TH = 0.16 mm (corresponding to the red curve in Fig. 2B). The wetting condition in the portion of the hydrophobic strip, which is uncovered by the air ring (width $w_{pho} - w_b$), is governed by the slip parameter $\beta$ ($0 \leq \beta \leq 1$). We have analyzed two conditions, namely, no slip ($\beta = 0$) and partial slip ($\beta = 0.043$, see section S4). The DR does not increase linearly with $w_{pho}$ due to the occurrence of the partial bubble contact on the hydrophobic strip. Instead, a maximum in the DR exists, supporting the experimental results of Fig. 4 (right).

on the hydrophilic strips ($\tau = \rho\upsilon(\frac{du_\theta}{dr} - \frac{u_\theta}{r})$) is larger than that on the surface of the equivalent smooth inner rotor (note that at the rotor surface, the term $\frac{u_\theta}{r}$ for comparing two cases is equal to $\Omega$). This is why the total DR is less than expected. Moreover, it can be inferred that there is a large azimuthal velocity gradient near the inner wall of the hydrophilic strips (*48*, *49*). When the air-water interface penetrates deeper into the gap flow, the azimuthal velocity gradient along the axial direction between the fluid flowing near the air rings and the water in the proximity of the hydrophilic strips, as well as the intensity of the Taylor vortexes, gets smaller (Fig. 6B). Accordingly, the momentum transport between the water above the hydrophilic strips and the air rings gets smaller, leading to an increase in DR with TH. Visualization of the flow scenarios of planar and patterned rotors at $R_{eC}$ = 1320 is provided in movie S1. The Taylor vortex axial position slightly varies along the azimuthal direction with time for both the smooth and patterned inner rotors. However, the intensity of the Taylor vortexes for the smooth inner rotor is stronger than that for the patterned inner rotor, which makes the ink strongly constrained by the Taylor vortexes on the smooth inner rotor.

For the TC flow generated using a smooth inner rotor, pairs of counter rotating vortexes, known as Taylor vortexes, form after a critical Reynolds number due to centrifugal instabilities (*50*). The axial length of each pair of vortexes (spatial period) is approximately 2*d* (*51*). When the air rings are introduced at the inner rotor surface, the intensity of the centripetal acceleration tends to have a periodical distribution because the azimuthal velocity in the flow has periodic gradients along the axial direction. The periodic centripetal acceleration causes new periodic vortex pairs, and the spatial period of these new vortex pairs is almost twice the period of the air rings. Moreover, because of the low air-solid friction, the total azimuthal momentum in the flow gets smaller. Thus, both the vorticity of the new vortex pairs and the azimuthal momentum transport in the radial direction decrease. This corresponds to the result that the exponent *n* in the measured torque scaling decreases from 1.44 to 1.32 (this can be referred to as "laminar shift").

Despite the fact that the air rings with different thickness are extremely stable in all the experiment conditions with Reynolds numbers up to 1320, corresponding to a rotating speed of 200 rpm (see section S6 and movie S2), we have also conducted an introductory study at one

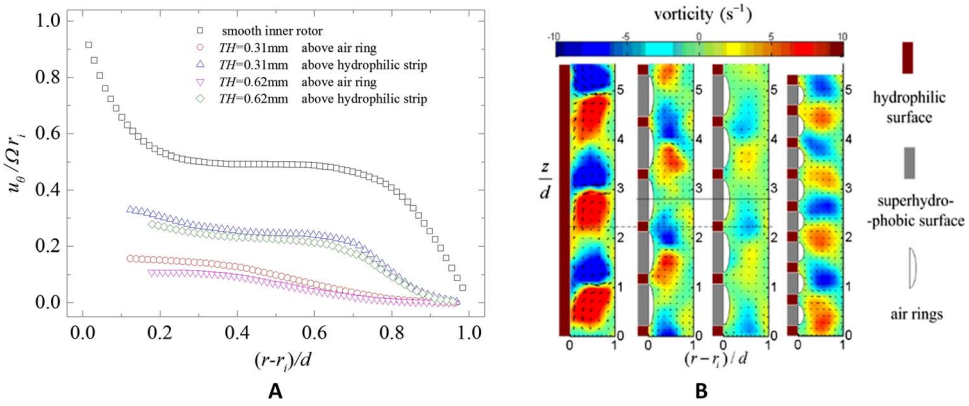


**Fig. 6. Experimental results showing the velocity profiles and vorticity fields for different texture configurations.** (**A**) Radial profiles of the mean azimuthal velocity. The radial position and the mean azimuthal velocity are normalized by the gap width and the rotation velocity of the inner rotor, which are $(r - r_i)/d$ and $u_\theta/\Omega r_i$, respectively. The mean azimuthal velocity profiles near the inner cylinder wall cannot be plotted because the measurements are impeded by the presence of the air rings. The horizontal solid line in (B) represents the axial position of the radial profile of the azimuthal velocity above the air ring. The dashed line in (B) represents the axial position of the radial profile of the azimuthal velocity above the hydrophilic strip. (**B**) Radial-axial vorticity fields of the gap flow measured at $Re_C = 660$. The axial position is normalized by the annular gap width, which is $z/d$. First column: smooth inner cylinder; second and third columns: TH = 0.31 mm and TH = 0.62 mm of the air rings with width of 4 mm; fourth column: TH = 0.31 mm of the air ring with width of 2 mm. Note that the bubble-wall water speed reduction (proportional to DR) obtained when increasing TH from 0.31 to 0.62 mm (red to pink points) is much smaller than the reduction encountered from TH = 0 to 0.31 mm (black to red points), in agreement with the theoretical predictions.

order of magnitude larger Reynolds numbers, therefore investigating the high turbulent regime, adopting a newly developed TC apparatus. The rig, not featuring a torque gauge in this initial realization, has an inner and an outer rotor with diameters of 50 and 70 mm, respectively, and the maximum rotating speed is 1500 rpm. It has been used to provide a preliminary investigation of the air ring stability in the high turbulent regime. In particular, we found that the TC flow in the presence of air rings experiences three markedly different regimes as the rotating speed is increased: (i) a stable-ring regime, (ii) a deformed-ring regime, and (iii) a ring-breakup regime (see movie S3). Further details will be provided in our follow-up contribution.

In conclusion, the newly designed alternated superhydrophobic and hydrophilic strips produce a large surface energy barrier at their junction zone and are responsible for the generation of annular air rings, which form a persistent continuous circumferential boundary along the flow direction in a TC flow configuration; this is responsible for the large DR measured in our apparatus. Because of the low dynamic viscosity of air, the air-solid friction in the air ring is small enough to be neglected. In the flow between the two cylindrical surfaces, there is a strong azimuthal momentum transport due to the viscous shear stress and Taylor vortexes, which leads to larger solid-water friction on the hydrophilic strips of the inner rotor with air rings than on the equivalent smooth inner rotor. Moreover, the momentum transport in the flow is strongly influenced by the location of the air-water interface in the gap between the cylinders; as a result, the total DR increases with the thickness of the air ring and approaches, but cannot reach, its maximum theoretical value. As the azimuthal velocity in the flow between the cylinders varies periodically with the strips in the axial direction, the centripetal acceleration, which controls the formation of the Taylor vortex, exhibits the same periodicity. As a result, not only the intensity of the Taylor vortex decreases but also its position and periodicity varies. The present work demonstrates the feasibility of a newly proposed design strategy that is capable of producing unprecedented DR efficiency by the optimized use of patterned superhydrophobicity/hydrophilicity. The proposed solution has significant application potential in designing novel DR devices, particularly in the marine sector and fluid transport and processing industries.

## METHODS

The total torque $T_m$ on the inner rotor was measured by a viscometer with a maximum rotating speed of 200 rpm (Brookfield Programmable LVDV-II+, Brookfield AMETEK, reproducibility error of ±0.2%). TC flow was created with a rotating inner rotor with radius $r_i = 12.5 \pm 0.02$ mm and a stationary outer cylinder with radius $r_o = 17 \pm 0.02$ mm. A schematic depiction of the apparatus is given in Fig. 1. The radius ratio $\eta = r_i/r_o$ was 0.74, and the gap between the cylinders $d = r_o - r_i$ was 4.5 mm. The height of the inner rotor was $L = 91 \pm 0.1$ mm, and the corresponding aspect ratio $\xi = L/(r_o - r_i)$ was 20.2. The gap between the cylinders was filled with air-saturated water at 25 ± 0.5°C. The height of the outer cylinder was $L_o = 111 \pm 0.1$ mm, whereas the gap between the bottoms of the inner and the outer cylinders was 10 ± 0.1 mm. The rotation rate of the inner rotor Ω was in the range of 10.47 to 20.93 rad/s, which lead to an attainable range of $Re_C$ between 660 and 1320. In this range of Reynolds numbers, by neglecting in first approximation the influence of the axial array of slippage areas on the TC regime boundaries, the TC flow regime was expected to be located in between wavy flow and modulated-wavy vortex flow (low-turbulent flow) (*47*, *52*, *53*). According to the empirical equations reported in section S5, the predicted ratio $T_b/T_m$ was 0.11 to 0.12. These values agree with the experimental finding. Finally, the rotor surface was either bare or processed with alternating annular superhydrophobic strips by masked spraying with a commercial paint (Ultra-Ever Dry, UltraTech International). The thickness of the superhydrophobic coating was 30 ± 3 μm, and the SEM of the jointed superhydrophobic and hydrophilic surfaces is shown in Fig. 1C.

To measure the shape of the air ring, a water bath tank of rectangular cross section was used in our experiments. The camera was set 30 cm away and normal to the cross section of the air rings. A scale plate was put 1 cm beside the air ring in its meridian plane. A panel light was used as background light to enhance the contrast between the air rings and

the water. The light projected to the air rings was reflected due to total reflection on the interface between air and water.

## SUPPLEMENTARY MATERIALS

Supplementary material for this article is available at http://advances.sciencemag.org/cgi/content/full/3/9/e1603288/DC1

section S1. Analytical model for the bubble ring

section S2. Estimation of the different contributions to drag and study of the stability of air rings and DR in the presence of surface grooves

section S3. On the flow regimes encountered in the experiments

section S4. Laminar flow dynamics and DR induced by the annular bubble theory

section S5. Torque contribution of the top and bottom cylinder flat surfaces

section S6. The dynamic stability of the air rings

fig. S1. Schematic representation of the bubble.

fig. S2. Results of the simulation of the bubble growth induced by air injection, for $w = 4.0$ mm, $r_i = 12.5$ mm, and zero rotational speed.

fig. S3. Results of the simulation: Dimensionless bubble pressure $p$ (black lines) and the dimensionless bubble axial length $w_b/w$ (red lines) as a function of the hydrophobic strip radial size $t_b$.

fig. S4. Results of the simulation: Dimensionless bubble pressure (black line) and bubble volume (red line) as a function of the dimensionless angular velocity.

fig. S5. Experimental results for the drag torque measurements with embedded circular bubbles.

fig. S6. Normalized cylinder torque $T/(\rho\upsilon^2 L)$ as a function of the Couette Reynolds number $Re_C$, in a log-log plot.

fig. S7. Normalized cylinder torque $T/(\rho\upsilon^2 L)$ as a function of the Couette Reynolds number $Re_C$, in a log-log plot.

fig. S8. Results of the simulation: Normalized cylinder torque $\bar{C}$ as a function of the slippage area density $\alpha$, for $\eta = 0.1$ (dotted line), $\eta = 0.5$ (dashed line), and $\eta = 0.735$ (solid line, referring to the experiments).

fig. S9. Results of the simulation.

fig. S10. Torque contribution of the top and bottom cylinder flat surfaces.

fig. S11. Air rings' dissolving process when the inner rotor is rotating in a 10 cm × 10 cm × 120 cm water tank.

movie S1. Visualization of the flow regimes of smooth and patterned rotors at ReC = 1320.

movie S2. Visualization of the stable air rings with different thickness in all the experiment conditions with Reynolds numbers up to 1320.

movie S3. Visualization of the air ring stability in the high turbulent regime, adopting a newly developed Taylor-Couette apparatus.

Reference (*54*)

## REFERENCES AND NOTES


1. S. L. Ceccio, Friction drag reduction of external flows with bubble and gas injection. *Annu. Rev. Fluid Mech.* **42**, 183–203 (2010).
2. J. P. Rothstein, Slip on superhydrophobic surfaces. *Annu. Rev. Fluid Mech.* **42**, 89–109 (2010).
3. C. M. White, M. G. Mungal, Mechanics and prediction of turbulent drag reduction with polymer additives. *Annu. Rev. Fluid Mech.* **40**, 235–256 (2008).
4. B. R. Elbing, S. Mäkiharju, A. Wiggins, M. Perlin, D. R. Dowling, S. L. Ceccio, On the scaling of air layer drag reduction. *J. Fluid Mech.* **717**, 484–513 (2013).
5. B. R. Elbing, E. S. Winkel, K. A. Lay, S. L. Ceccio, D. R. Dowling, M. Perlin, Bubble-induced skin-friction drag reduction and the abrupt transition to air-layer drag reduction. *J. Fluid Mech.* **612**, 201–236 (2008).
6. Y. Murai, H. Oiwa, Y. Takeda, Frictional drag reduction in bubbly Couette-Taylor flow. *Phys. Fluids* **20**, 034101 (2008).
7. W. C. Sanders, E. S. Winkel, D. R. Dowling, M. Perlin, S. L. Ceccio, Bubble friction drag reduction in a high-Reynolds-number flat-plate turbulent boundary layer. *J. Fluid Mech.* **552**, 353–380 (2006).
8. T. H. van den Berg, S. Luther, D. P. Lathrop, D. Lohse, Drag reduction in bubbly Taylor-Couette turbulence. *Phys. Rev. Lett.* **94**, 044501 (2005).
9. K. Fukuda, J. Tokunaga, T. Nobunaga, T. Nakatani, T. Iwasaki, Y. Kunitake, Frictional drag reduction with air lubricant over a super-water-repellent surface. *J. Mar. Sci. Technol.* **5**, 123–130 (2000).
10. E. L. Amromin, B. Metcalf, G. Karafiath, Synergy of resistance reduction effects for a ship with bottom air cavity. *J. Fluid Eng.* **133**, 021302 (2011).
11. S. A. Mäkiharju, B. R. Elbing, A. Wiggins, S. Schinasi, J.-M. Vanden-Broeck, M. Perlin, D. R. Dowling, S. L. Ceccio, On the scaling of air entrainment from a ventilated partial cavity. *J. Fluid Mech.* **732**, 47–76 (2013).
12. M. Callenaere, J.-P. Franc, J.-M. Michel, M. Riondet, The cavitation instability induced by the development of a re-entrant jet. *J. Fluid Mech.* **444**, 223–256 (2001).
13. K. A. Lay, R. Yakushiji, S. Makiharju, M. Perlin, S. L. Ceccio, Partial cavity drag reduction at high Reynolds numbers. *J. Ship Res.* **54**, 109–119 (2010).
14. C.-H. Choi, C.-J. Kim, Large slip of aqueous liquid flow over a nanoengineered superhydrophobic surface. *Phys. Rev. Lett.* **96**, 066001 (2006).
15. P. Joseph, C. Cottin-Bizonne, J.-M. Benoît, C. Ybert, C. Journet, P. Tabeling, L. Bocquet, Slippage of water past superhydrophobic carbon nanotube forests in microchannels. *Phys. Rev. Lett.* **97**, 156104 (2006).
16. M. Nosonovsky, Material science: Slippery when wetted. *Nature* **477**, 412–413 (2011).
17. J. Ou, B. Perot, J. P. Rothstein, Laminar drag reduction in microchannels using ultrahydrophobic surfaces. *Phys. Fluids* **16**, 4635 (2004).
18. J. Ou, J. P. Rothstein, Direct velocity measurements of the flow past drag-reducing ultrahydrophobic surfaces. *Phys. Fluids* **17**, 103606 (2005).
19. F. Schellenberger, N. Encinas, D. Vollmer, H.-J. Butt, How water advances on superhydrophobic surfaces. *Phys. Rev. Lett.* **116**, 096101 (2016).
20. S. Srinivasan, J. A. Kleingartner, J. B. Gilbert, R. E. Cohen, A. J. B. Milne, G. H. McKinley, Sustainable drag reduction in turbulent Taylor-Couette flows by depositing sprayable superhydrophobic surfaces. *Phys. Rev. Lett.* **114**, 014501 (2015).
21. E. Aljallis, M. A. Sarshar, R. Datla, V. Sikka, A. Jones, C.-H. Choi, Experimental study of skin friction drag reduction on superhydrophobic flat plates in high Reynolds number boundary layer flow. *Phys. Fluids* **25**, 025103 (2013).
22. J. Hyväluoma, J. Harting, Slip flow over structured surfaces with entrapped microbubbles. *Phys. Rev. Lett.* **100**, 246001 (2008).
23. T. G. Min, J. Kim, Effects of hydrophobic surface on skin-friction drag. *Phys. Fluids* **16**, L55 (2004).
24. A. Steinberger, C. Cottin-Bizonne, P. Kleimann, E. Charlaix, High friction on a bubble mattress. *Nat. Mater.* **6**, 665–668 (2007).
25. E. Karatay, A. S. Haase, C. W. Visser, C. Sun, D. Lohse, P. A. Tsai, R. G. H. Lammertink, Control of slippage with tunable bubble mattresses. *Proc. Natl. Acad. Sci. U.S.A.* **110**, 8422–8426 (2013).
26. C. Lee, C.-H. Choi, C.-J. Kim, Structured surfaces for a giant liquid slip. *Phys. Rev. Lett.* **101**, 064501 (2008).
27. C. Lee, C.-J. Kim, Maximizing the giant liquid slip on superhydrophobic microstructures by nanostructuring their sidewalls. *Langmuir* **25**, 12812–12818 (2009).
28. D. Song, R. J. Daniello, J. P. Rothstein, Drag reduction using superhydrophobic sanded Teflon surfaces. *Exp. Fluids* **55**, 1783 (2014).
29. C. Ybert, C. Barentin, C. Cottin-Bizonne, P. Joseph, L. Bocquet, Achieving large slip with superhydrophobic surfaces: Scaling laws for generic geometries. *Phys. Fluids* **19**, 123601 (2007).
30. L. Bertocchi, D. Dini, M. Giacopini, M. T. Fowell, A. Baldini, Fluid film lubrication in the presence of cavitation: A mass-conserving two-dimensional formulation for compressible, piezoviscous and non-Newtonian fluids. *Tribol. Int.* **67**, 61–71 (2013).
31. S. Medina, M. T. Fowell, S.-C. Vladescu, T. Reddyhoff, I. Pegg, A. V. Olver, D. Dini, Transient effects in lubricated textured bearings. *Proc. Inst. Mech. Eng. Part J* **229**, 523–537 (2015).
32. M. Scaraggi, Lubrication of textured surfaces: A general theory for flow and shear stress factors. *Phys. Rev. E* **86**, 026314 (2012).
33. M. Scaraggi, Textured surface hydrodynamic lubrication: Discussion. *Tribol. Lett.* **48**, 375–391 (2012).
34. D. Saranadhi, D. Chen, J. A. Kleingartner, S. Srinivasan, R. E. Cohen, G. H. McKinley, Sustained drag reduction in a turbulent flow using a low-temperature Leidenfrost surface. *Sci. Adv.* **2**, e1600686 (2016).
35. B. J. Rosenberg, T. Van Buren, M. K. Fu, A. J. Smits, Turbulent drag reduction over air- and liquid-impregnated surfaces. *Phys. Fluids* **28**, 015103 (2016).
36. D. Bonn, J. Eggers, J. Indekeu, J. Meunier, E. Rolley, Wetting and spreading. *Rev. Mod. Phys.* **81**, 739 (2009).
37. J. F. Joanny, P. G. de Gennes, A model for contact-angle hysteresis. *J. Chem. Phys.* **81**, 552 (1984).
38. Y. Zheng, H. Bai, Z. Huang, X. Tian, F.-Q. Nie, Y. P. Zhao, J. Zhai, L. Jiang, Directional water collection on wetted spider silk. *Nature* **463**, 640–643 (2010).
39. M. Musterd, V. van Steijn, C. R. Kleijn, M. T. Kreutzer, Droplets on inclined plates: Local and global hysteresis of pinned capillary surfaces. *Phys. Rev. Lett.* **113**, 066104 (2014).
40. C. Semprebon, M. Brinkmann, On the onset of motion of sliding drops. *Soft Matter* **10**, 3325–3334 (2014).
41. H.-J. Butt, C. Semprebon, P. Papadopoulos, D. Vollmer, M. Brinkmann, M. Ciccotti, Design principles for superamphiphobic surfaces. *Soft Matter* **9**, 418–428 (2013).
42. X. Tian, T. Verho, R. H. A. Ras, Moving superhydrophobic surfaces toward real-world applications. *Science* **352**, 142–143 (2016).

43. A. Busse, N. D. Sandham, G. McHale, M. I. Newton, Change in drag, apparent slip and optimum air layer thickness for laminar flow over an idealised superhydrophobic surface. *J. Fluid Mech.* **727**, 488–508 (2013).
44. F.-M. Chang, S.-J. Hong, Y. J. Sheng, H.-K. Tsao, Wetting invasion and retreat across a corner boundary. *J. Phys. Chem. C* **114**, 1615–1621 (2010).
45. R. Poetes, K. Holtzmann, K. Franze, U. Steiner, Metastable underwater superhydrophobicity. *Phys. Rev. Lett.* **105**, 166104 (2010).
46. A. J. Greidanus, R. Delfos, J. Westerweel, Drag reduction by surface treatment in turbulent Taylor-Couette flow. *J. Phys. Conf. Ser.* **318**, 082016 (2011).
47. E. Bilgen, R. Boulos, Functional dependence of torque coefficient of coaxial cylinders on gap width and Reynolds-numbers. *J. Fluid Eng.* **95**, 122–126 (1973).
48. P. S. Marcus, Simulation of Taylor-Couette flow. Part 2. Numerical results for wavy-vortex flow with one travelling wave. *J. Fluid Mech.* **146**, 65–113 (1984).
49. K. Nakabayashi, Z. M. Zheng, Y. Tsuchida, Evolution of mean and fluctuating velocity components in the laminar–turbulent transition of spherical Couette flow. *Phys. Fluids* **14**, 2839 (2002).
50. C. D. Andereck, S. S. Liu, H. L. Swinney, Flow regimes in a circular Couette system with independently rotating cylinders. *J. Fluid Mech.* **164**, 155–183 (1986).
51. A. Akonur, R. M. Lueptow, Three-dimensional velocity field for wavy Taylor–Couette flow. *Phys. Fluids* **15**, 947 (2003).
52. J. T. Stuart, On the non-linear mechanics of hydrodynamic stability. *J. Fluid Mech.* **4**, 1–21 (1958).
53. S. Grossmann, D. Lohse, C. Sun, High–Reynolds number Taylor-Couette turbulence. *Annu. Rev. Fluid Mech.* **48**, 53–80 (2016).
54. S. Harmand, J. Pelle, S. Poncet, I. V. Shevchuk, Review of fluid flow and convective heat transfer within rotating disk cavities with impinging jet. *Int. J. Therm. Sci.* **67**, 1 (2013).



**Acknowledgments**

**Funding:** This research was financially supported by the National Natural Science Foundation of China (51679203, 51335010, 21434009, and 11372305) and the Natural Science Basic Research Plan in Shaanxi Province of China (2016JM1002). D.D. would also like to acknowledge the support received from the Engineering and Physical Sciences Research Council under Established Career Fellowship grant EP/N025954/1. **Author contributions:** H.H., D.D., and F.Z. proposed the idea. H.H., J.W., and L.B. performed the experiment and drafted the paper. L.B., L.J., D.S., B.S., G.P., and Q.X. discussed the experiment results. M.S. and D.D. performed simulation. H.H., J.W., M.S., D.D., and F.Z. discussed the results and revised the paper. **Competing interests:** The authors declare that they have no competing interests. **Data and materials availability:** All data needed to evaluate the conclusions in the paper are present in the paper and/or the Supplementary Materials. Additional data related to this paper may be requested from the corresponding authors: huhaibao@nwpu.edu.cn, d.dini@imperial.ac.uk, and zhouf@licp.cas.cn.

Submitted 27 December 2016
Accepted 4 August 2017
Published 1 September 2017
10.1126/sciadv.1603288

**Citation:** H. Hu, J. Wen, L. Bao, L. Jia, D. Song, B. Song, G. Pan, M. Scaraggi, D. Dini, Q. Xue, F. Zhou, Significant and stable drag reduction with air rings confined by alternated superhydrophobic and hydrophilic strips. *Sci. Adv.* **3**, e1603288 (2017).

# Significant and stable drag reduction with air rings confined by alternated superhydrophobic and hydrophilic strips

Haibao Hu, Jun Wen, Luyao Bao, Laibing Jia, Dong Song, Baowei Song, Guang Pan, Michele Scaraggi, Daniele Dini, Qunji Xue and Feng Zhou

*Sci Adv* **3** (9), e1603288.
DOI: 10.1126/sciadv.1603288